Numerical Study of Droplet Evaporation in a High-Temperature Stream

M. Renksizbulut[1]

M. C. Yuen
Professor and Chairman.
Mem. ASME

Department of Mechanical and Nuclear Engineering,
Northwestern University,
Evanston, Ill. 60201

Numerical solutions for high-temperature air flowing past water and methanol droplets and solid spheres, and superheated steam flowing past water droplets were obtained in the Reynolds number range of 10 to 100. The coupled momentum, energy, and specie continuity equations of variable thermophysical properties were solved using finite difference techniques. The numerical results of heat transfer and total drag agree well with existing experimental data. Mass transfer decreases friction drag significantly but at the same time increases pressure drag by almost an equal amount. The net effect is that the standard drag curve for solid spheres can be used for evaporating droplets provided the density is the free stream density and the viscosity of the vapor mixture is evaluated at an appropriate reference temperature and concentration. Both the mass efflux and variable properties decrease heat transfer rates to the droplets.

1 Introduction

This paper describes an attempt to study theoretically a high-temperature gas flow past an evaporating liquid droplet. As such it is in sequel to our experimental measurements of heat and mass transfer from liquid droplets in a high temperature air stream [1].

Flow past a sphere in the intermediate Reynolds number range of 10 to 100 is of interest in many fields of engineering. For a uniform free stream, the flow field is axisymmetrical and steady. However, in this Reynolds number range, the Navier-Stokes equations cannot be simplified and numerical methods have to be used. The variable-property case is difficult enough that only a few attempts have been made to study the problem.

In his pioneering work, Jenson [2] solved the Navier-Stokes equations for a constant-property flow past a sphere in the stream function/vorticity formulation for Reynolds numbers between 5 and 40. The finite-difference equations were correct to second order in grid spacing. Since ψ and ω vary most rapidly near the droplet, variable grid spacing is desirable with finer mesh near the sphere and coarser mesh far away. Jenson accomplished this with the coordinate transformation $r=e^{\xi}$ which has been adopted in almost all subsequent studies.

Much work has been done to extend and improve on the work by Jenson. These include studies by Hamielec, Hoffman, and Ross [3], Rimon and Cheng [4], LeClair, Hamielec, and Pruppacher [5], Woo and Hamielec [6], and Rivkind, Ryskin, and Fishbein [7]. Similar efforts by Dennis and Walker [8], and Dennis, Walker, and Hudson [9], using a series truncation method, were also successful in solving the problem of flow past a sphere, including heat transfer, up to a Reynolds number of 40. The results obtained by different investigators show reasonably good agreement with one another and also with related experimental correlations for heat transfer and drag.

The study of the variable-property problem in the past was limited to the low Reynolds number flows ($Re << 1$) using the method of matched asymptotic expansions. This included the work of Chang [10], Kassoy, Adamson, and Messiter [11], and Fendell, Coats, and Smith [12]. More recently, Sayegh and Gauvin [13] numerically solved the coupled momentum and energy equations for variable-property heat transfer to a solid sphere in high-temperature surroundings. Their results are for Pr = .67, Re between 0.1 and 50, and T_d^*/T_s^* = .25, .5, .75 and 1. The constant-property solutions ($T_d^*/T_s^*=1$) are in good agreement with the literature, but their variable property solutions show negative pressure drag coefficients for $Re \geq 20$ with T_d^*/T_s^* = .25. Harpole [14] investigated both variable-property and blowing effects from evaporation on axisymmetric stagnation point flows. He assumed that the ratio of solutions with and without evaporation is the same for the stagnation point flow and flow past a sphere.

The present study is focussed on flow past a single component liquid droplet in a high-temperature environment at intermediate Reynolds numbers. A finite difference scheme is used to solve the coupled momentum, energy, and species equations. The numerical results are compared with the drag data of Yuen and Chen [15] and heat transfer data of Renksizbulut and Yuen [1].

For a high-temperature gas flow past a liquid droplet, the effect of evaporation is twofold. Firstly, the mass efflux changes the flow field which directly affects the drag and heat transfer. Secondly, evaporation keeps the droplet at the wet-bulb temperature which is generally much lower than the free stream temperature. At the same time the evaporating specie changes the gas composition near the droplet. The drag data of reference [15] indicates that the net effect of evaporation can be taken into account by the change in the thermophysical properties. On the other hand, the data of [1] indicates that both mass efflux and variable property effects reduce heat transfer. The present numerical study is undertaken to

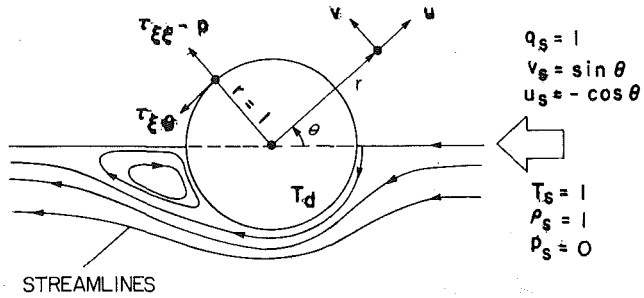

Fig. 1 Schematic of flow past an evaporating droplet

[1] Present address: Westinghouse Canada, Inc., Hamilton, Ontario, Canada L8N 3K2

Contributed by the Heat Transfer Division for publication in the JOURNAL OF HEAT TRANSFER. Manuscript received by the Heat Transfer Division February 5, 1982.

develop a better understanding of the physics of the problem and to give a successful numerical scheme to calculate variable-property heat transfer and drag of evaporating droplets.

2 Mathematical Formulation

A schematic of the flow past an evaporating droplet is shown in Fig. 1. The equations describing the flow include the conservation equations of mass, momentum, energy, and specie for both the gas and liquid phases. Additional equations are the equation of state and other thermodynamic and transport relationships. In order to make the problem tractable, the following assumptions are made:

1 The gas phase is assumed to be a binary mixture of ideal gases of equal molecular weights and equal and constant specific heats. Only Fick's law of diffusion and Fourier heat conduction are considered.

2 It is assumed that the gas-phase processes are quasi-steady. This is justified by the fact that the gas-phase heat and mass transport rates are of the order of 10^{-4}-10^{-5} m^2/s which are much larger than the surface regression rates of 10^{-7}-10^{-8} m^2/s. The numerical calculations of Hubbard, Denny, and Mills [16] have substantiated this assumption.

3 Liquid phase motion and core heating are neglected. The droplet temperature remains uniformly at the wet-bulb temperature and the vapor pressure of the evaporating specie is the equilibrium vapor pressure corresponding to the wet-bulb temperature. Liquid phase motion is induced by the gas phase motion. At atmospheric pressure, the liquid phase motion is of the order of one-hundredth of the gas phase motion. This value is further reduced by the presence of interfacial surface contaminants. In fact, for all the drag measurements of water droplets in air, the drag coefficients are the same as that of solid spheres. Law and Sirignano [17] have shown that at atmospheric pressure, core heating is a small fraction of the energy budget after the initial 10-20 percent of the lifetime of a droplet. For a single component liquid, temperature distribution and liquid phase motion do not affect heat transfer as long as core heating is negligible. Thus, unsteadiness and coupling between liquid and gas phase processes due to liquid motion and core heating can be neglected for a single component liquid at low or moderate pressures. This, however, is not true for high-pressure evaporation or for multicomponent liquid as shown by Prakash and Sirignano [18, 19].

4 Effects of gravity, chemical reaction, viscous dissipation, compressibility, turbulence, and thermal radiation are neglected.

5 The flow field is axisymmetric. For constant-property flow, this symmetry starts to deteriorate at the onset of wake instability ($Re_s \simeq 130$).

The governing equations are nondimensionalized with respect to the free stream quantities and the radius of the sphere as indicated in the nomenclature. With the coordinate transformation, $r = -\xi^{-1}$, and by introducing the stream function and vorticity as

$$\rho u \sin\theta = \xi^2 \frac{\partial \psi}{\partial \theta},$$

$$\rho v \sin\theta = \xi^3 \frac{\partial \psi}{\partial \xi},$$

$$\omega = \xi^3 \frac{\partial}{\partial \xi}\left(\frac{v}{\xi}\right) + \xi \frac{\partial u}{\partial \theta} \tag{1}$$

it is possible (see [20]) to express the governing equations in the following unified format

$$a_\phi \xi^2 \left[\frac{\partial}{\partial \xi}\left(\phi \frac{\partial \psi}{\partial \theta}\right) - \frac{\partial}{\partial \theta}\left(\phi \frac{\partial \psi}{\partial \xi}\right)\right] - \xi^2 \frac{\partial}{\partial \xi}\left[b_\phi \sin\theta \frac{\partial}{\partial \xi}(c_\phi \phi)\right]$$

$$- \frac{\partial}{\partial \theta}\left[b_\phi \sin\theta \frac{\partial}{\partial \theta}(c_\phi \phi)\right] + d_\phi \xi^{-2} \sin\theta = 0 \tag{2}$$

where $\phi(\xi, \theta)$ is used as a generalized variable to represent T, Y, ψ, or $\Omega = -\omega\xi/\sin\theta$, and the equation of state is given by $\rho T = 1$. The first term in equation (2) is the convection term, the second and third terms are diffusion terms, and the last one is the source term. The corresponding coefficient functions a_ϕ, b_ϕ, c_ϕ, and d_ϕ are given in Appendix A.

The boundary conditions are

$$\xi = -1: \quad T = T_d, \; Y = Y_d,$$

$$\frac{\partial \psi}{\partial \theta} = \frac{2k \sin\theta}{\mathrm{Re}_s \mathrm{Pr}_s L_d}\left(\frac{\partial T}{\partial \xi}\right),$$

$$\Omega = \frac{1}{\rho \sin^2\theta}\left\{2\frac{\partial \psi}{\partial \xi} - \frac{\partial^2 \psi}{\partial \xi^2} - \frac{\partial^2 \psi}{\partial \theta^2} + \left(\frac{\partial \psi}{\partial \theta}\right)\cot\theta\right\} \tag{3}$$

Nomenclature

a^* = radius of sphere
B = mass transfer number, $c_p^*(T_s^* - T_d^*)/L^*$
C_D = total drag coefficient, $F_D^*/(\pi a^{*2} \rho_s^* q_s^{*2}/2)$
C_F = friction drag coefficient, $F_F^*/(\pi a^{*2} \rho_s^* q_s^{*2}/2)$
C_P = pressure drag coefficient, $F_P^*/(\pi a^{*2} \rho_s^* q_s^{*2}/2)$
C_T = thrust coefficient, $F_T^*/(\pi a^{*2} \rho_s^* q_s^{*2}/2)$
c_p^* = heat capacity
D = mass diffusivity, (D^*/D_s^*)
d^* = diameter of sphere
F^* = force
h^* = heat transfer coefficient
k = thermal conductivity, (k^*/k_s^*)
L = heat of vaporization, $L^*/(c_p^* T_s^*)$
$\dot{m}$ = mass transfer rate, $\dot{m}^*/(a^{*2} \rho_s^* q_s^*)$
Nu = Nusselt number, $(h^* d^*/k^*)$
p = pressure, $(p^* - p_s^*)/(\rho_s^* q_s^{*2}/2)$
Pr = Prandtl number, $(c_p^* \mu^*/k^*)$
q^* = velocity
r = radial coordinate, (r^*/a^*)
Re = Reynolds number, $(\rho^* q^* d^*/\mu^*)$
Re_s = $\rho_s^* q_s^* d^*/\mu_s^*$
Re_M = $\rho_s^* q_s^* d^*/\mu_f^*$
Re_t = $\rho_s^* q_s^* d^*/\mu_t^*$
T = temperature, (T^*/T_s^*)
u = velocity in r-direction, (u^*/q_s^*)
v = velocity in θ-direction, (v^*/q_s^*)
Y = mass fraction of evaporating specie
Z = $[\mathrm{Nu}(1+B)^{0.7} - 2]\mathrm{Pr}^{-1/3}$
δ = boundary layer thickness, (δ^*/d^*)
θ = angular coordinate
μ = viscosity coefficient, (μ^*/μ_s^*)
ξ = modified radial coordinate, $(-r^{-1})$
ρ = density, (ρ^*/ρ_s^*)
τ = stress tensor, $\tau^*/(\mu_s^* q_s^*/a^*)$
ψ = stream function, $\psi^*/(\rho_s^* q_s^* a^{*2})$
Ω = modified vorticity, $\omega/(r\sin\theta)$
ω = vorticity, $\omega^*/(q_s^* a^*)$
ϕ = generalized variable, T, Y, ψ or Ω

Superscript

* = dimensional quality
$\bar{}$ = averaged quantity

Subscript

d = droplet surface
f = film condition
o = stagnation point
s = free-stream condition
t = one-third reference state

Table 1 Summary of problems studied numerically

Case	Description	Re_s	Pr_s	T_s^*(K)	T_d^*(K)	Y_s	Y_d	B
1	Water-steam	100, 70, 40, 20, 10,	.986	600	373	1.0	1.0	.204
2	Water-steam		1.01	800	373	1.0	1.0	.407
3	Water-steam		1.02	1000	373	1.0	1.0	.783
4	Methanol-air		.869	800	331	0.0	.766	.462
5	Water-air		.869	800	353	0.0	.355	.213
6	Solid sph.-air		.700	$T_d - T_s \to 0$		0	0	0
7	Solid sph.-air		.680	600	340	0	0	0
8	Solid sph.-air		.689	800	353	0	0	0

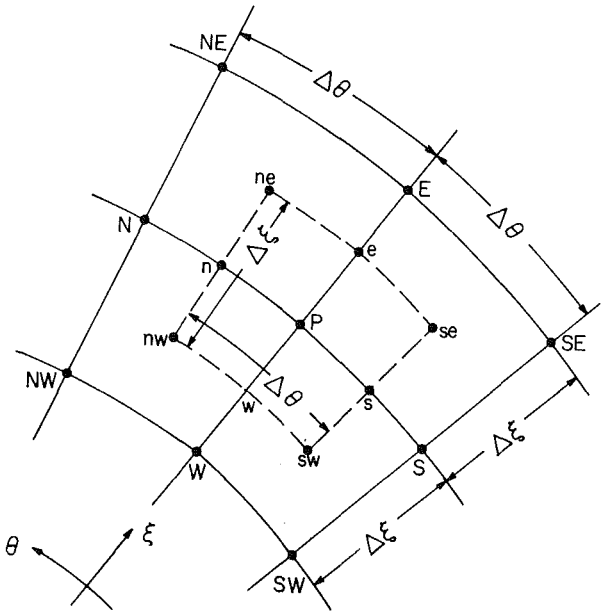

Fig. 2 The finite-difference grid

$\xi \to 0$: $T \to 1$, $Y \to 0$, $\Omega \to 0$,

$$\psi \to -\frac{\sin^2\theta}{2\xi^2} + \frac{\dot{m}}{4\pi}(1-\cos\theta) \tag{4}$$

The heat transfer to the sphere can be expressed as the local and averaged Nusselt numbers

$$\mathrm{Nu}_d = \frac{2k_d}{(1-T_d)}\left(\frac{\partial T}{\partial \xi}\right)_d \tag{5}$$

$$\overline{\mathrm{Nu}} = \frac{1}{2}\int_0^\pi \mathrm{Nu}_d \sin\theta d\theta \tag{6}$$

The drag forces acting on the sphere can be expressed in terms of the drag coefficients

$$C_F = \frac{8}{\mathrm{Re}_s}\int_0^\pi (\tau_{\xi\theta,d}\sin\theta - \tau_{\xi\xi,d}\cos\theta)\sin\theta d\theta \tag{7}$$

where

$$\tau_{\xi\theta,d} = \left[-\mu\Omega\sin\theta + \frac{2\mu}{\rho\sin\theta}\left(2\frac{\partial\psi}{\partial\xi} - \frac{\partial^2\psi}{\partial\xi^2}\right)\right]_d$$

$$\tau_{\xi\xi,d} = \left[-\frac{4\mu}{\rho\sin\theta}\left(\frac{\partial\psi}{\partial\theta}\right)\left(1+\frac{1}{3\rho}\frac{\partial\rho}{\partial\xi}\right)\right]_d$$

$$C_P = \int_0^\pi p_d \sin(2\theta)\, d\theta \tag{8}$$

$$C_T = \int_0^\pi 2\rho_d u_d^2 \sin(2\theta)\, d\theta \tag{9}$$

$$C_D = C_F + C_P + C_T \tag{10}$$

In order to determine the pressure distribution on the droplet surface, first the radial momentum equation is integrated along the leading axis ($\theta = 0$) to obtain the stagnation pressure (p_0). Next, the surface pressure (p_d) is calculated by integrating the tangential momentum equation from the stagnation point along the droplet surface. The equations for the stagnation pressure and the surface pressure are

$$p_0 = 1 - (\rho u^2)_0 - \frac{16}{3\mathrm{Re}_s}\left(\frac{\mu u}{\rho}\frac{\partial\rho}{\partial\xi}\right)_0 - \int_{-1}^{0}\left(u^2\frac{\partial\rho}{\partial\xi}\right)_{\theta=0} d\xi$$

$$+ \frac{8}{\mathrm{Re}_s}\int_{-1}^{0}\left[-\frac{\mu}{\xi}\frac{\partial\omega}{\partial\theta} - \frac{\partial\mu}{\partial\xi}\left(\frac{\partial u}{\partial\xi} + \frac{u}{\rho}\frac{\partial\rho}{\partial\xi}\right)\right]_{\theta=0}\xi^2 d\xi \tag{11}$$

$$p_d = p_0 + \int_0^\theta\left[\frac{2}{\sin^2\theta}\frac{\partial\psi}{\partial\theta}\xi^2\frac{\partial}{\partial\xi}\xi^2\frac{\partial\psi}{\partial\xi} + \frac{4}{\mathrm{Re}_s}\left\{\mu\left(\omega + \xi^2\frac{\partial\omega}{\partial\xi}\right)\right.\right.$$

$$\left. - \xi^2\frac{\partial\mu}{\partial\xi}\left(\omega + \frac{2}{\rho\sin\theta}\xi^2\frac{\partial}{\partial\xi}\xi^2\frac{\partial\psi}{\partial\xi}\right) - \frac{4\mu}{3}\frac{\partial}{\partial\theta}\left(\frac{\xi^2}{\rho^2\sin\theta}\right.\right.$$

$$\left.\left.\left.\frac{\partial\psi}{\partial\theta}\frac{\partial\rho}{\partial\xi}\right)\right\}\right]_{\xi=-1} d\theta \tag{12}$$

Further details can be found in [21].

3 Numerical Method

The generalized governing equations as represented by equation (2) are solved using a finite difference method, the main features of which follow [20]. In Fig. 2, a typical element of the finite difference grid is shown. The central node is P and the four surrounding nodes which are equally spaced are identified with E, W, N and S. Equation (2) is discretized using second-order central differences. The exception is in the convective term where the "upstream" differencing principle is introduced. The result is a successive substitution formula

$$\phi_P = C_E\phi_E + C_W\phi_W + C_N\phi_N + C_S\phi_S + D_P \tag{13}$$

where C_E, C_W, C_N, C_S and D_P are defined in Appendix B.

For numerical analysis, the conditions along the axis have to be specified, they are

$\theta = 0$:
$$\psi = \frac{\partial T}{\partial\theta} = \frac{\partial Y}{\partial\theta} = 0,\ \Omega = -\xi\frac{\partial\omega}{\partial\theta} \tag{14}$$

$\theta = \pi$:
$$\frac{\partial T}{\partial\theta} = \frac{\partial Y}{\partial\theta} = 0,\ \Omega = \xi\frac{\partial\omega}{\partial\theta},$$

$$\psi = \frac{\dot{m}}{2\pi} = \int_0^\pi\left[\frac{2k\sin\theta}{\mathrm{Re}_s\mathrm{Pr}_s L_d}\left(\frac{\partial T}{\partial\xi}\right)\right]_d d\theta \tag{15}$$

The numerical task is to solve simultaneously $4N$ nonlinear algebraic equations as given by equation (13) where N is the total number of grid points in the flow field. These equations will be solved using successive overrelaxation coupled with the Gauss-Seidel method. The iterative process is as follows:

1 Initially, all ϕ and the boundary conditions are specified.

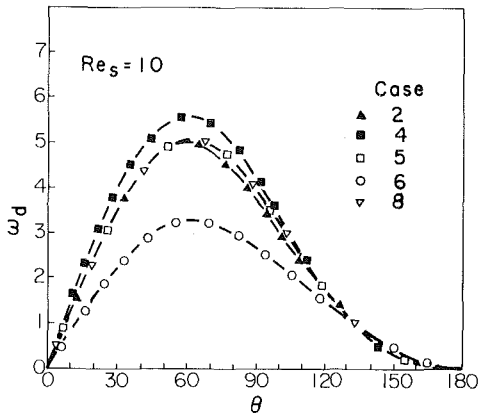

Fig. 3 Surface vorticity distributions for $Re_S = 10$. Case numbers are listed in Table 1.

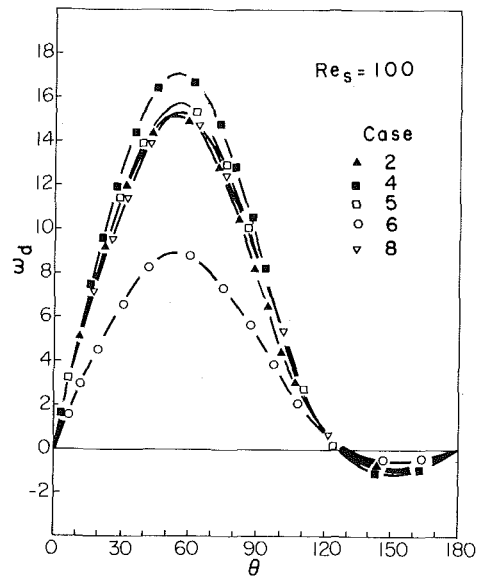

Fig. 4 Surface vorticity distributions for $Re_S = 100$. Case numbers are listed in Table 1.

2 Each cycle of iteration consists of four subcycles corresponding to solving equation (13), and hence equation (2), for Ω, ψ, T, and Y in the order stated.

3 Overrelaxation parameters in the range between 1 and 1.5 are used to increase the rate of convergence of the iterative scheme.

4 Convergence is assumed in the Kth iteration when

$$[1 - \phi_P{}^{(K-1)}/\phi_P^{(K)}]_{\max} \sim 10^{-4}$$

Iterative schemes such as the present one do not always converge to a stable and physically meaningful solution. No convergence criterion exists for the nonlinear algebraic system (equation (13)) under consideration. However, well-known convergence conditions for linear systems can be used as guide-lines, and compliance with such criteria may be considered as a minimum requirement for stability.

A detailed study by Varga [22] shows that the linearized algebraic version of equation (13) (i.e., constant C_E, C_W, C_N, C_S, and D_P) satisfy the convergence criteria with the upwind differencing scheme. Although the present numerical scheme satisfies the linearized convergence criteria, the numerical scheme may still diverge if C's and D_P exhibit large variations from one iteration to the next. Such a problem is likely to arise in the early stages of the computation process particularly if the initial guesses are poor. Divergence problems were not encountered in the present work.

While the upwind-difference scheme assures convergence for convection dominated flow, under certain conditions, it is responsible for large truncation errors to generate a false diffusion effect which tends to reinforce real diffusion. If this occurs, the grid spacing may have to be reduced to the extent that it renders the computation uneconomical. Further investigation as given in reference [21] indicates that the consequences of false diffusion is most serious in the flow where the molecular diffusion is important relative to forced convection and also where the streamline is not parallel to one of the grid lines. With the present grid spacing of $\Delta\xi = .025$ and $\Delta\theta = 3$ deg, the only region where false diffusion effect is important is the wake region. Thus the exact location of the flow separation point or the exact size of the recirculation zone cannot be determined with the same accuracy as the rest of the flow variables. However, the integrated results such as drag and heat transfer coefficients are not much affected because it is only at higher Reynolds numbers that the contribution to momentum and heat transfer from the wake region becomes significant. For example Frössling's [23] experimental results on the evaporation of naphthalene spheres in air show that at Reynolds numbers below 550, heat transfer rates to the wake region of the spheres are less than 12 percent of the overall transfer rates.

Some attempts were made to adopt the exponential differencing scheme to suppress the false diffusion effect. This method was first proposed by Allen and Southwell [24] and a recent analysis is given by Chow and Tien [25]. The present study shows that for the variable-property problems under consideration, this technique is not superior to the present method. This is partly due to the longer computation times associated with exponential functions. More importantly perhaps is that the assumption of conservation of directional flux is violated in the variable property case by the presence of the source term, D_p, in equation (13).

4 Results and Discussion

Numerical solutions for air flowing past solid spheres, water, and methanol droplets, and steam flowing past water droplets were obtained up to a Reynolds number of 100. The range of the numerical solutions are summarized in Table 1. All computations were carried out using the grid spacings of $\Delta\xi = .025$ and $\Delta\theta = 3$ deg. Solutions obtained with smaller radial grid spacing ($\Delta\xi = 0.0165$) showed negligible improvement at the expense of much longer computation times. The free stream boundary conditions were applied at $r = 40$. Convergence is assumed when the maximum fractional change in the calculated variables, ϕ_P, after K iterations (typically $K \sim 350$ steps) was of order 10^{-4} for all independent variables.

The transport coefficients of air and steam were approximated by $\mu = T^{.67}$, $k = T^{.81}$ and $\mu = kT$, respectively. For water and methanol droplets evaporating in air, it was assumed that $\rho D = T$, and the mixture viscosity and thermal conductivity were computed using Wilke's rule [26] subject to the equal molecular weight assumption. In all cases, the fluid density varied with temperature as $\rho = 1/T$. The constant specific heat assumption leads to $B = (1 - T_d)/L_d$. The isothermal condition is $T_d = 1$. For solid spheres, B is equal to zero in all cases.

(a) The Flow Field. The surface vorticity, ω_d, distributions for $Re_s = 10$ and 100 are given in Figs. 3 and 4. Both figures show that the surface vorticity values increase with decreasing T_d for the solid sphere. This can be seen from the fact that $\omega_d \sim 1/\delta$ where δ is the dimensionless thickness of the viscous layer. Generally, $1/\delta \sim (\rho\ Re_s/\mu)^{1/2}$, and, therefore, the properties that influence ω_d are ρ/μ. As T_d decreases, i.e., the surface gets colder, the surface ρ increases and μ decreases resulting in an increase in ω_d. This also holds

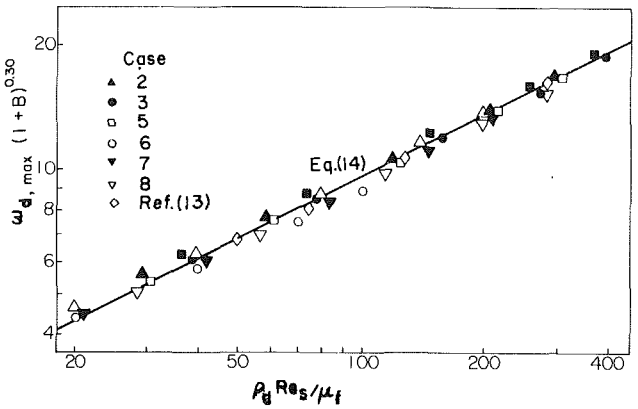

Fig. 5 Maximum vorticity correlation. Case numbers are listed in Table 1 except as noted.

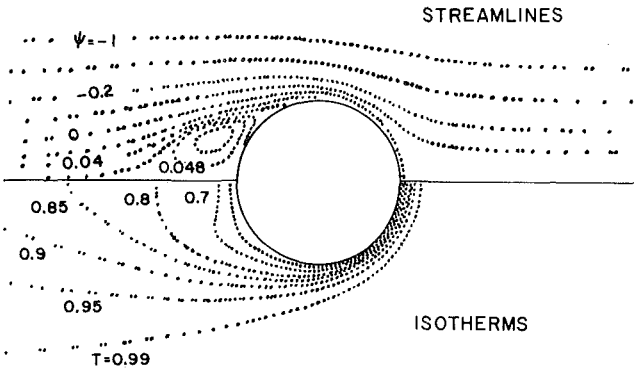

Fig. 6 Stream function and isotherms of methanol droplets in air for $T_s = 800$ K, $T_d = 0.414$, and $Re_s = 100$

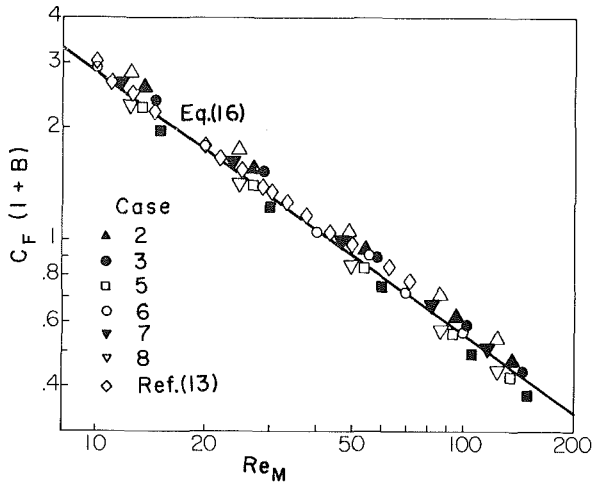

Fig. 7 Friction drag correlation. Case numbers are listed in Table 1 except as noted.

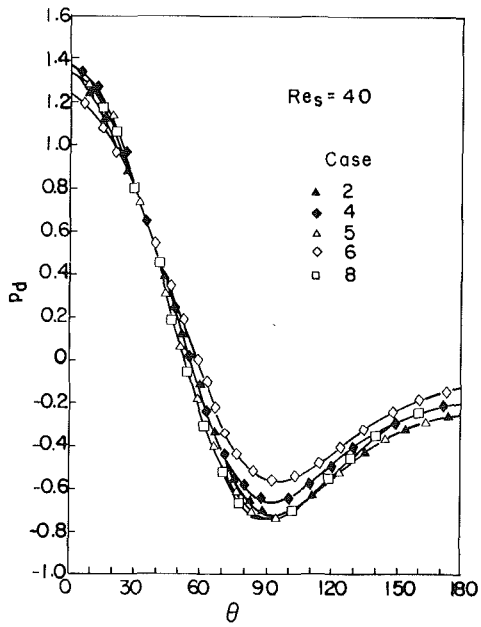

Fig. 8 Surface pressure distribution for $Re_s = 40$. Case numbers are listed in Table 1.

true for evaporating droplets. Mass efflux from the evaporating droplet directly increases δ and reduces ω_d. However, the viscosity coefficient of mixtures of air and vapor are generally lower than that of air at the same temperature resulting in a larger increase in ω_d. For the same T_d, these two effects tend to cancel each other and the resulting surface vorticity levels for the solid sphere and evaporating sphere are about the same.

Figures 3 and 4 further show that the location of $\omega_{d,max}$ is at about $\theta = 60$ deg relatively independent of Reynolds number, fluid properties, and evaporation rate. The correlation of $\omega_{d,max}$ as a function of Reynolds and B numbers is shown in Fig. 5. The numerical results correlate well with the following equation

$$\omega_{d,max}(1+B)^{0.30} = 0.97(\rho_d Re_s/\mu_f)^{0.50} \quad (16)$$

where the subscript f refers to the film condition defined by $r = 1/2$ in the following equations

$$T_r^* = T_d^* + r(T_s^* - T_d^*), \quad Y_r = Y_d + r(Y_s - Y_d) \quad (17)$$

The surface vorticity distributions given by [3] for $Re_s = 100$ with constant fluid properties and prescribed asymmetric blowing ($B \simeq 4$) show a 40 percent reduction in $\omega_{d,max}$. For the same B number, equation (16) predicts a 38 percent reduction in $\omega_{d,max}$ due to mass transfer alone. This good agreement suggests that the accuracy of the blowing correction term $(1+B)^{0.3}$ is not limited to the relatively low B numbers encountered in the present work. With regard to variable-property effects, a limited number of data points available from [13] for solid spheres show excellent agreement with the present results as can be seen in Fig. 5.

In Fig. 6, the upper half shows the stream lines and the lower half shows the isotherms for a methanol sphere in a free stream air of 800 K and a Reynolds number of 100. As shown in the figure, several stream lines originate from the sphere due to evaporation. The wake behind the sphere is no longer a closed wake as there is some leakage near the axis ($\theta = \pi$). The isotherms show steep gradients at the front stagnation point, indicating that heat transfer rate is much higher at the front half of the sphere.

(b) Drag. The friction drag coefficients as a function of mass transfer numbers and Reynolds numbers are shown in Fig. 7. The numerical data of C_F correlates well with the equation

$$C_F(1+B) = 14.5\ Re_M^{-.71} \quad (18)$$

where Re_M is defined as $\rho_s^* q_s^* d^*/\mu_f^*$. Equation (18) shows that mass transfer plays a significant role in reducing friction drag. In the case of a flat plate, the reduction in the friction drag coefficient by evaporation was shown by Emmons [27] to be $(1+B)^{-.75}$ for B below 4. Further reduction in C_F occurs due to lower fluid viscosity ($\mu < 1$) within the cold boundary layer

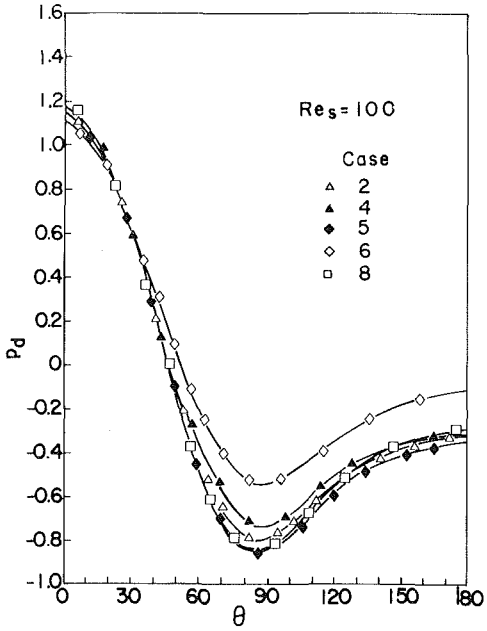

Fig. 9 Surface pressure distribution for $Re_s = 100$. Case numbers are listed in Table 1.

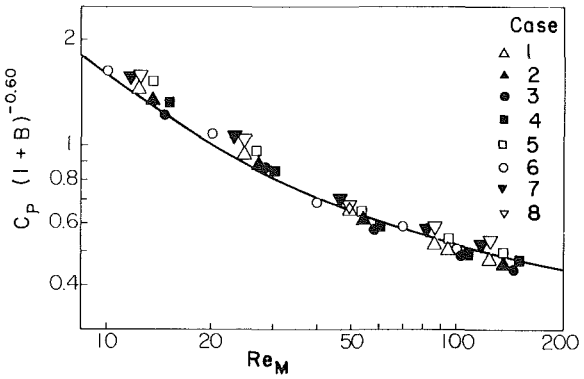

Fig. 10 Pressure drag correlation. Case numbers are listed in Table 1.

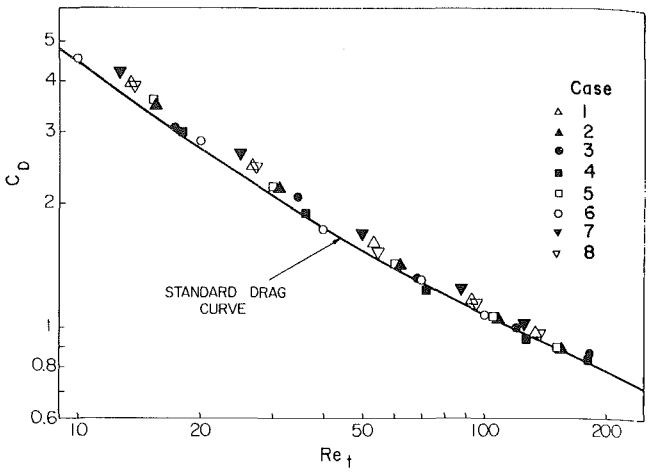

Fig. 11 Total drag correlation. Case numbers are listed in Table 1.

which is reflected through the Reynolds number definition, Re_M. Friction drag coefficients obtained from reference [13] for solid spheres ($B=0$) are also shown in Fig. 7 as a function of Re_M. The agreement with equation (18) is good.

Figures 8 and 9 show surface pressure distributions for $Re_s = 40$ and 100. These figures indicate that the surface pressure generally decreases with decreasing T_d, except for a small region near the stagnation point. From the surface pressure distribution, the pressure drag coefficient (C_p) can be computed using equation (8). The results are shown in Fig. 10 as a function of Reynolds and mass transfer numbers. Figure 10 indicates that for the same free stream conditions, C_p depends on both B and μ_f^* for evaporating droplets, but it depends only on μ_f^* for solid spheres. For evaporating droplets, the effect of mass efflux is to increase C_p by a factor of $(1+B)^{0.6}$ for the same Re_M. The mixture viscosity coefficient of an evaporating droplet is lower than that of pure air at the same temperature. Therefore, for the same free stream conditions and droplet temperature, Re_M of an evaporating droplet is larger than Re_M of a solid sphere. It follows that the ordinate of Fig. 10 of an evaporating droplet is smaller than that of a solid sphere. However, this does not necessarily mean that C_p of an evaporating droplet is smaller. For $T_d < 1$, B is greater than zero for an evaporating droplet. Depending on the magnitude of B, C_p of an evaporating droplet can even be larger. Detailed calculations as shown in [21] indicate that c_p of an evaporating droplet is actually larger than a corresponding solid sphere at the same free stream conditions and T_d.

In addition to pressure and shear forces, an evaporating droplet experiences a net thrust due to asymmetric blowing at its surface. The computed thrust coefficients, C_T, show that the values are at least two orders of magnitude smaller than the corresponding C_F and C_P values and are therefore neglected.

Figure 11 shows that the computed total drag coefficient C_D values correlate well with the standard drag curve without the need for a B number correction provided that the Reynolds number is defined as $Re_f = \rho_s^* q_s^* d^*/\mu_f^*$ where μ_f^* is the mixture viscosity based on the one-third reference state ($r = 1/3$ in equation (17)). Since this type of correlation was originally suggested in [15] based on their experimental data as well as those of Eisenklam, Arunchalam, Weston [28], it means that the present numerical results are in good agreement with experimental data. In the Reynolds number range of 10 to 260, it is also possible to correlate the results as

$$C_D (1+B)^{0.20} = \frac{24}{Re_M}[1 + .2\, Re_M^{0.63}] \tag{19}$$

This correlation agrees satisfactorily with experimental data as shown in Fig. 12.

(c) Heat Transfer. The surface distributions of the local Nusselt numbers, Nu_d, are shown in Figs. 13 and 14 for $Re_s = 10$ and 100. As expected, much higher heat transfer rates are observed over the leading half of the sphere particularly near the front stagnation point. It is also observed that both the blowing and variable-property effects decrease Nu with decreasing T_d. The numerical results of [13] indicate similar reductions in local transfer rates which are entirely due to variable fluid properties.

At a given Reynolds number, the local temperature gradient on the droplet surface becomes steeper as T_d is reduced either by increasing the free-stream temperature or by lowering the surface temperature. Normally, this would lead to a higher heat transfer rate. However, due to the cold boundary effect, such reduction in T_d is accompanied by a large reduction in the local thermal conductivity of the gas. The present results as well as those of [13] indicate that the effect of decrease in thermoconductivity of the gas outweighs the effect of increase in temperature gradient such that the local heat transfer rate decreases.

In the case of an evaporating droplet, the vapor leaving the surface opposes the flow of hot gas toward the surface resulting in a thicker thermal boundary layer. Furthermore, pure steam and, mixtures of water and methanol vapors with

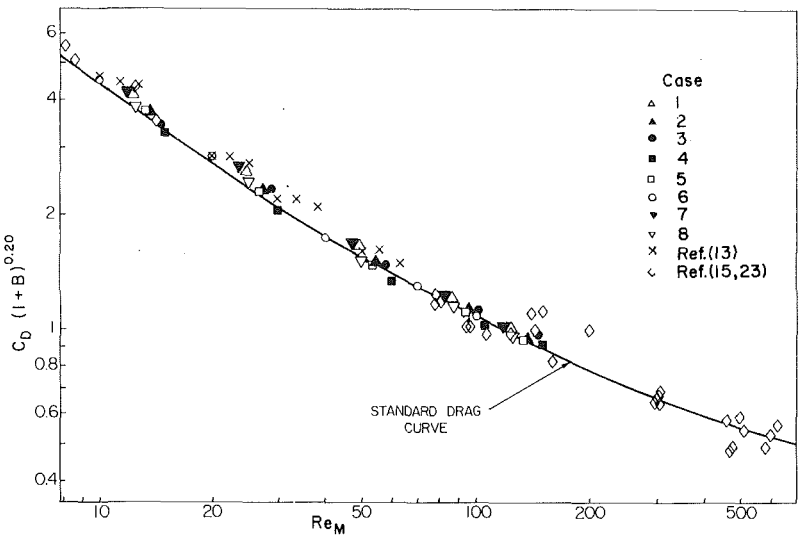

Fig. 12 Total drag correlation. Case numbers are listed in Table 1 except as noted.

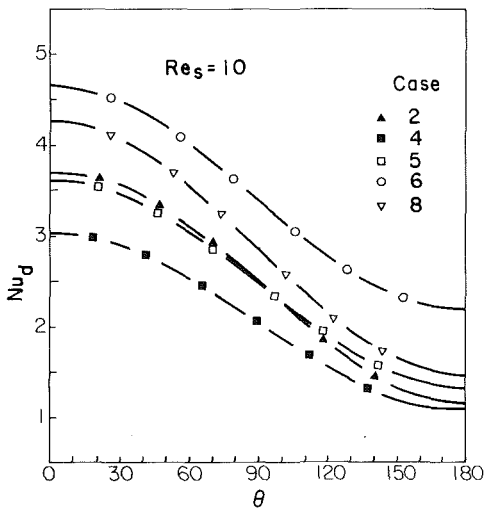

Fig. 13 Surface Nusselt number distributions for $Re_S = 10$. Case numbers are listed in Table 1.

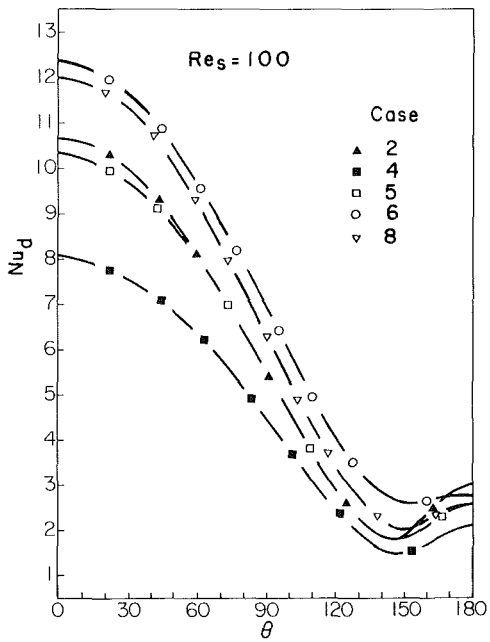

Fig. 14 Surface Nusselt number distribution for $Re_S = 100$. Case numbers are listed in Table 1.

air have lower thermal conductivities than pure air at the same temperature; therefore, the cold boundary effect on thermal conductivity is even more pronounced. Hence, both blowing and variable property effects reinforce one another in reducing heat transfer rates to droplets.

The present numerically calculated stagnation point Nusselt numbers, Nu_o, are shown in Fig. 15 as a function of Reynolds, Prandtl and B numbers. It is seen that the results correlate quite well with the equation

$$Z_{o,f} = [Nu_{o,f}(1+B)^{0.70} - 2]Pr_f^{-1/3} = 0.90Re_M^{0.57} \quad (20)$$

in the Re_M range from 10 to 150. Thus, equation (20) indicates that mass transfer reduces stagnation-point heat transfer by a factor of $(1+B)^{0.70}$. Also shown in Fig. 15 are the numerical results of [13] and [14] for solid spheres in air, and water droplets in superheated steam, respectively. The three sets of results agree well with each other.

The most recent experimental correlation of heat transfer for evaporating droplets in air, as shown in [1], is

$$Z_f = [\overline{Nu}_f(1+B)^{0.70} - 2]Pr_f^{-1/3} = 0.57\ Re_M^{1/2} \quad (21)$$

In Fig. 16, the present numerical results are compared with equation (21). The numerical data of [13] for solid spheres are also included in the same figure. The agreement is satisfactory (within about 15 percent), considering the fact that there is

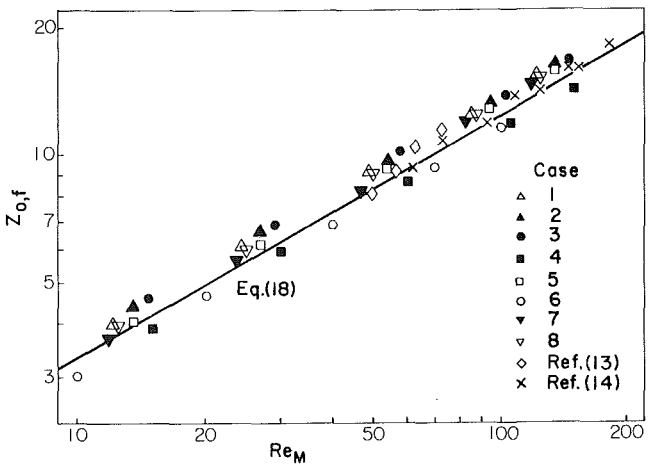

Fig. 15 Numerical stagnation-point heat transfer data. Case numbers are listed in Table 1 except as noted.

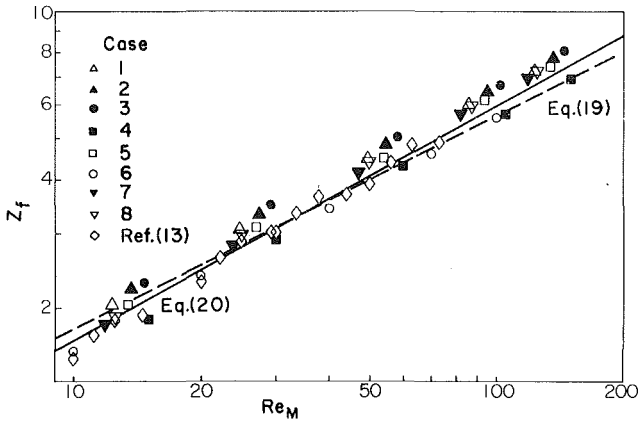

Fig. 16 Numerical heat transfer data. Case numbers are listed in Table 1 except as noted.

considerable scattering among the numerical data. It appears that a better fit to the data in the Re_M range from 10 to 150 is

$$Z_f = 0.48\ Re_M^{0.55} \tag{22}$$

Presently it is not clear whether the 15 percent discrepancy is the result of some of the simplifying assumptions or perhaps numerical inaccuracy or perhaps both.

Conclusion

Numerical solutions for variable-property flows past solid and liquid droplets were obtained in the Reynolds number range of 10 to 100 with free-stream temperatures up to 1000 K. The numerical values of heat transfer and drag agree well with the existing experimental data. The results detail the effects of mass efflux and variable properties on drag and heat transfer. Mass efflux directly reduces friction drag by a factor of $(1+B)$, but increases pressure drag by a factor of $(1+B)^6$. The net effect on total drag is that the standard drag curve can be used for both evaporating and solid droplets provided the characteristic density is the free-stream density and the characteristic viscosity is evaluated using the 1/3 rule ($r=1/3$ in equation (15)). Both the mass efflux and variable properties decrease heat transfer to the droplet. The numerically calculated average Nusselt numbers agree with experimental data to within 15 percent.

Acknowledgment

This research was supported by NSF and Northwestern University.

References

1 Renksizbulut, M., and Yuen, M. C., "Experimental Study of Droplet Evaporation in a High Temperature Air Stream," ASME JOURNAL OF HEAT TRANSFER, Vol. 105, No. 2, May 1983, pp. 384-388.

2 Jenson, V. G., "Viscous Flow Round a Sphere at Low Reynolds Numbers, (<40)," *Proc. Royal Soc.*, Vol. 249A, 1959, pp. 346-366.

3 Hamielec, A. E., Hoffman, T. W., and Ross, L. L., "Numerical Solution of the Navier-Stokes Equation for Flow Past Spheres, Part 1: Viscous Flow Around Spheres With and Without Radial Mass Efflux," *AIChE Journal*, Vol. 13, 1967, pp. 212-224.

4 Rimon, J., and Cheng, S. I., "Numerical Solution of a Uniform Flow Over a Sphere at Intermediate Reynolds Numbers," *Phys. Fluids*, Vol. 12, 1969, pp. 949-959.

5 Le Clair, B. P., Hamielec, A. E., and Pruppacher, H. R., "A Numerical Study of the Drag on a Sphere at Low and Intermediate Reynolds Numbers," *J. Atmos. Sci.*, Vol. 27, 1970, pp. 308-315.

6 Woo, S. E., and Hamielec, A. E., "A Numerical Method of Determining the Rate of Evaporation of Small Water Drops Falling at Terminal Velocity in Air," *J. Atmos. Sci.*, Vol. 28, 1971, pp. 1448-1454.

7 Rivkind, V., Ryskin, G. M., and Fishbein, G. A., "Flow Around a Spherical Drop at Intermediate Reynolds Numbers," *Appl. Math. Mech.*, Vol. 40, 1976, pp. 687-691.

8 Dennis, S. C. R., and Walker, J. D. A., "Calculation of the Steady Flow Past a Sphere at Low and Moderate Reynolds Numbers," *Journal of Fluid Mechanics*, 1971, Vol. 48, pp. 771-789.

9 Dennis, S. C. R., Walker, J. D. A., and Hudson, J. D., "Heat Transfer From a Sphere at Low Reynolds Numbers," *Journal of Fluid Mechanics*, Vol. 60, 1973, pp. 273-283.

10 Chang, I.-D., "Slow Motion of a Sphere in a Compressible Viscous Fluid," *J. Appl. Math. Phys.*, Vol. 16, 1965, pp. 449-469.

11 Kassoy, D. R., Adamson, T. C. Jr., and Messiter, A. F., "Compressible Low Reynolds Number Flow Around a Sphere," *Phys. Fluids*, Vol. 9, 1966, pp. 671-681.

12 Fendell, F. E., Coats, D. E., and Smith, E. B., "Compressible Slow Viscous Flow Past a Vaporizing Droplet," *AIAA Journal*, Vol. 6, 1968, pp. 1953-1960.

13 Sayegh, N. N., and Gauvin, W. H., "Numerical Analysis of Variable Property Heat Transfer to a Single Sphere in High Temperature Surroundings," *AIChE Journal*, Vol. 25, 1979, pp. 522-534.

14 Harpole, G. M., "Droplet Evaporation in High Temperature Environments," ASME JOURNAL OF HEAT TRANSFER, Vol. 103, 1981, pp. 86-91.

15 Yuen, M. C., and Chen, L. W., "On Drag of Evaporating Liquid Droplets," *Combustion Sci. Tech.*, Vol. 14, 1976, pp. 147-154.

16 Hubbard, G. L., Denny, V. E., and Mills, A. F., "Droplet Evaporation: Effects of Transients and Variable Properties," *International Journal of Heat and Mass Transfer*, Vol. 18, 1975, pp. 1003-1008.

17 Law, C. K., and Sirignano, W. A., "Unsteady Droplet Combustion with Droplet Heating—II: Conduction Limit," *Combustion and Flame*, Vol. 28, 1977, pp. 175-186.

18 Prakash, S., and Sirignano, W. A., "Liquid Fuel Droplet Heating With Internal Circulation," *International Journal of Heat and Mass Transfer*, Vol. 21, 1978, pp. 885-895.

19 Prakash, S., and Sirignano, W. A., "Theory of Convective Droplet Vaporization With Unsteady Heat Transfer in the Circulating Liquid Phase," *International Journal of Heat and Mass Transfer*, Vol. 23, 1980, pp. 253-268.

20 Gosman, A. D., Pun, W. M., Runchal, A. K., Spalding, D. B., and Wolfshtein, M., *Heat and Mass Transfer in Recirculating Flows*, Academic Press, London, 1969.

21 Renksizbulut, M., "Energetics and Dynamics of Droplet Evaporation in High-Temperature Intermediate Reynolds Number Flows," Ph.D. dissertation, Northwestern University, Evanston, Ill., 1981.

22 Varga, R. S., *Matrix Iterative Analysis*, Prentice-Hall International, London, 1962.

23 Frössling, N., "Uber die Verdungtung Fallenden Tropfen," *Gerlands Beitr. Geophys.*, Vol. 52, 1938, pp. 170-216.

24 Allen, D. N. G., and Southwell, R. V., "Relaxation Methods Applied to Determine the Motion, in Two Dimensions, of a Viscous Fluid Past a Fixed Cylinder," *Quart. J. Mech. Appl. Math.*, Vol. 8, 1955, pp. 129-145.

25 Chow, L. C., and Tien, C. L., "An Examination of Four Differencing Schemes for Some Elliptic-Type Convection Equations," *Num. Heat Transfer*, Vol. 1, 1978, pp. 87-100.

26 Wilke, C. R., "A Viscosity Equation for Gas Mixtures," *J. Chem. Phys.*, Vol. 18, 1950, pp. 517-519.

27 Emmons, H. W., "The Film Combustion of Liquid Fuel," *ZAMM*, Vol. 36, 1956, pp. 60-71.

28 Eisenklam, P., Arunachalam, S. A., and Weston, J. A., "Evaporation Rates and Drag Resistance of Burning Drops," *Eleventh International Symposium on Combustion*, 1967, pp. 715-728.

APPENDIX A
Coefficient Functions Associated With Equation (2)

ϕ	a_ϕ	b_ϕ	c_ϕ	d_ϕ
Ω	$.5\ Re_s \xi^{-2}\sin^2\theta$	$\xi^{-2}\sin^2\theta$	μ	d_Ω†
ψ	0	$\xi^2/(\rho\sin^2\theta)$	1	$-\Omega$
T	$.5\ Re_s Pr_s$	k/c_p	1	0
Y	$.5\ Re_s Sc_s$	ρD	1	0

†$d_\Omega = 2\xi^2\sin\theta((Re_s P/4)-S)$,

$$P=\frac{\partial\rho}{\partial\xi}\left(u\frac{\partial u}{\partial\theta}+v\frac{\partial v}{\partial\theta}\right)-\frac{\partial\rho}{\partial\theta}\left(u\frac{\partial u}{\partial\xi}+v\frac{\partial v}{\partial\xi}\right)$$

$$S=\left[\xi\frac{\partial\mu}{\partial\xi}\left(v\cot^2\theta-2\xi\frac{\partial v}{\partial\xi}-\frac{\partial v}{\partial\theta}\cot\theta-\frac{\partial^2 v}{\partial\theta^2}-\frac{\partial u}{\partial\theta}\right.\right.$$

$$\left.+\xi\frac{\partial^2 u}{\partial\xi\partial\theta}-\frac{\Omega\sin\theta}{\xi^2}\right)+\frac{\partial\mu}{\partial\theta}\left(u-\xi\frac{\partial u}{\partial\xi}-\xi^2\frac{\partial^2 u}{\partial\xi^2}\right.$$

$$+v\cot\theta+\xi\frac{\partial v}{\partial\xi}\cot\theta+\xi\frac{\partial^2 v}{\partial\xi\partial\theta}\Big)-\xi^2\frac{\partial^2\mu}{\partial\xi^2}\Big(\frac{\Omega\sin\theta}{\xi^2}$$

$$+\xi\frac{\partial v}{\partial\xi}\Big)+\xi\frac{\partial^2\mu}{\partial\theta^2}\frac{\partial v}{\partial\xi}-\xi\frac{\partial^2\mu}{\partial\xi\partial\theta}\Big(u+\frac{\partial v}{\partial\theta}+\xi\frac{\partial u}{\partial\xi}\Big)\Big]$$

APPENDIX B
Coefficient Functions Associated With Equation (13)

$$C_i=(A_i+B_ic_{\phi,i})/G;i=\mathrm{E, W, N, S}$$

$$D_P=-\Delta\xi\Delta\theta d_{\phi,P}\sin\theta_P/(G\xi_P^2),$$

$$G=A_\mathrm{E}+A_\mathrm{W}+A_\mathrm{N}+A_\mathrm{S}+c_{\phi,P}(B_\mathrm{E}+B_\mathrm{W}+B_\mathrm{N}+B_\mathrm{S}),$$

$$A_\mathrm{E}=\frac{1}{8}a_{\phi,P}\xi_P^2[(\psi_{\mathrm{SE}}+\psi_\mathrm{S}-\psi_{\mathrm{NE}}-\psi_\mathrm{N})+|\psi_{\mathrm{SE}}+\psi_\mathrm{S}-\psi_{\mathrm{NE}}-\psi_\mathrm{N}|],$$

$$A_\mathrm{W}=\frac{1}{8}a_{\phi,P}\xi_P^2[(\psi_{\mathrm{NW}}+\psi_\mathrm{N}-\psi_{\mathrm{SW}}-\psi_\mathrm{S})+|\psi_{\mathrm{NW}}+\psi_\mathrm{N}-\psi_{\mathrm{SW}}-\psi_\mathrm{S}|],$$

$$A_\mathrm{N}=\frac{1}{8}a_{\phi,P}\xi_P^2[(\psi_{\mathrm{NE}}+\psi_\mathrm{E}-\psi_{\mathrm{NW}}-\psi_\mathrm{W})+|\psi_{\mathrm{NE}}+\psi_\mathrm{E}-\psi_{\mathrm{NW}}-\psi_\mathrm{W}|],$$

$$A_\mathrm{S}=\frac{1}{8}a_{\phi,P}\xi_P^2[(\psi_{\mathrm{SW}}+\psi_\mathrm{W}-\psi_{\mathrm{SE}}-\psi_\mathrm{E})+|\psi_{\mathrm{SW}}+\psi_\mathrm{W}-\psi_{\mathrm{SE}}-\psi_\mathrm{E}|],$$

$$B_\mathrm{E}=\frac{1}{2}\xi_P^2\sin\theta_P\Big(\frac{\Delta\theta}{\Delta\xi}\Big)(b_{\phi,\mathrm{E}}+b_{\phi,P}),$$

$$B_\mathrm{W}=\frac{1}{2}\xi_P^2\sin\theta_P\Big(\frac{\Delta\theta}{\Delta\xi}\Big)(b_{\phi,\mathrm{W}}+b_{\phi,P}),$$

$$B_\mathrm{N}=\frac{1}{4}\Big(\frac{\Delta\xi}{\Delta\theta}\Big)(b_{\phi,N}+b_{\phi,P})(\sin\theta_\mathrm{N}+\sin\theta_P),$$

$$B_\mathrm{S}=\frac{1}{4}\Big(\frac{\Delta\xi}{\Delta\theta}\Big)(b_{\phi,S}+b_{\phi,P})(\sin\theta_\mathrm{S}+\sin\theta_P)$$